Excited-State Optically Detected Magnetic Resonance of Spin Defects in Hexagonal Boron Nitride

Zhao Mu,[1,*] Hongbing Cai,[1,*] Disheng Chen,[1] Jonathan Kenny,[1] Zhengzhi Jiang,[2] Shihao Ru,[1] Xiaodan Lyu,[1] Teck Seng Koh,[1] Xiaogang Liu,[2] Igor Aharonovich,[3,4,†] and Weibo Gao[1,5,‡]

[1]*Division of Physics and Applied Physics, School of Physical and Mathematical Sciences, Nanyang Technological University, Singapore 637371, Singapore*

[2]*Department of Chemistry, National University of Singapore, Singapore 117543, Singapore*

[3]*School of Mathematical and Physical Sciences, University of Technology Sydney, Ultimo, New South Wales 2007, Australia*

[4]*ARC Centre of Excellence for Transformative Meta-Optical Systems, University of Technology Sydney, Ultimo, New South Wales 2007, Australia*

[5]*The Photonics Institute and Centre for Disruptive Photonic Technologies, Nanyang Technological University, Singapore 637371, Singapore*

(Received 27 January 2022; revised 24 March 2022; accepted 27 April 2022; published 27 May 2022)

Negatively charged boron vacancy (V_B^-) centers in hexagonal boron nitride (h-BN) are promising spin defects in a van der Waals crystal. Understanding the spin properties of the excited state (ES) is critical for realizing dynamic nuclear polarization. Here, we report zero-field splitting in the ES of $D_{ES} = 2160$ MHz and its associated optically detected magnetic resonance (ODMR) contrast of 12% at cryogenic temperature. In contrast to nitrogen vacancy (NV^-) centers in diamond, the ODMR contrast of V_B^- centers is more prominent at cryotemperature than at room temperature. The ES has a g factor similar to the ground state. The ES photodynamics is further elucidated by measuring the level anticrossing of the V_B^- defects under varying external magnetic fields. Our results provide important information for utilizing the spin defects of h-BN in quantum technology.

DOI: 10.1103/PhysRevLett.128.216402

Color centers with optically addressable spins in wide band gap materials (e.g., diamond [1,2] and silicon carbide [3,4]) have been intensively studied in recent decades for applications in quantum sensing [5–8] and quantum information processing [9,10]. For nanoscale sensing, it is preferable to bring the sensor close to the investigated object to enhance sensitivity [11–13]. Spin qubits in 2D materials naturally meet this requirement and present an extra opportunity for quantum sensing besides the remarkable spatial resolution and sensitivity achieved by diamond nitrogen vacancy (NV^-) centers [14,15].

Among various 2D materials, hexagonal boron nitride (h-BN) has attracted much attention for its capability to exhibit various bright single-photon emitters at room temperature (RT) [16–18]. In addition, recent discoveries of optically addressable spin defects have further boosted the efforts to investigate these defects for quantum sensing applications [19–24]. In particular, the negatively charged boron vacancy (V_B^-) defect is of great interest due to its known molecular structure and reliable engineering methods [20,25–30].

The V_B^- center consists of a boron vacancy surrounded by three nitrogen atoms and an extra electron captured from the environment [Fig. 1(a)]. The spin-spin interaction along the out-of-plane direction splits the triplet ground state into $m_s = 0$ and $m_s = \pm 1$ manifolds with a zero-field splitting (ZFS) of $D_{GS} = 3460$ MHz at RT [Fig. 1(b)] [20,31,32]. The ground state optically detected magnetic resonance

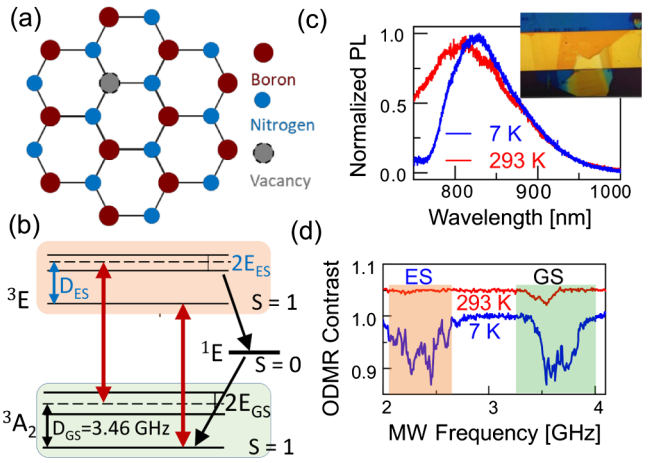

FIG. 1. (a) Schematic of a V_B^- defect in h-BN. (b) Energy structures of V_B^- centers. It consists of a triplet ground state ($^3A_2$), a triplet excited state (^3E), and a singlet state (^1E). (c) Photoluminescence (PL) spectra of V_B^- centers excited with 532 nm light at 293 K (red) and 7 K (blue). Inset: the microscopic image of the exfoliated h-BN on a 50 μm wide gold stripline. (d) GS ODMR (light green shadow) and ES ODMR (light gold shadow) of the V_B^- defects at 293 and 7 K. The curves are vertically shifted for clarity.

(GS ODMR) contrast of ensemble V_B^- centers can reach up to 46%, making it appealing for quantum applications [25]. The V_B^- centers have been employed to sense temperature, pressure, and magnetic fields [33]. Thanks to the 2D nature of the host, these sensors are also used for the in-site imaging of the magnetic properties of layered materials by constructing van der Waals heterostructures [34]. The excited state of the V_B^- centers is crucial in mediating the interaction between the electron spins and the nearby nuclear spins [35,36]. Although the excited state of this system has been predicted to be a triplet [31,32], the exact configurations of these energy levels are still unknown.

In this Letter, we investigated the excited state ODMR (ES ODMR) spectrum of V_B^- centers at cryogenic temperatures. The magnetic field-dependent ES ODMR revealed an excited triplet state with a longitudinal splitting of $D_{ES} \sim 2160$ MHz, and a g factor of ~2. The D_{ES} was also substantiated by approaching the ES $m_s = 0$ and $m_s = -1$ state under an external magnet, giving an emission minimum near the excited-state level anticrossing (ESLAC) point at ~800 G (~2240 MHz).

For sample preparation, a 50 μm wide straight gold stripline was first deposited on the Si/SiO_2 substrate before the exfoliated h-BN was transferred to the stripline. This wide stripline ensures the generation of a homogeneous in-plane magnetic field at the center of the line for spin manipulations [25]. We then bombarded the h-BN with Ga^+ ions at the center and edge of the gold line. The h-BN flake on the stripline is shown in Fig. 1(c) (inset). The detailed sample preparation method is described in Supplemental Material, Sec. A [37]. Typical luminescence spectra of the V_B^- ensembles at 293 and 7 K are shown in Fig. 1(c). The emission was collected into a multimode fiber via a homebuilt confocal microscope before being directed into a spectrometer or photon counting device. The stripline was wire bonded to a chip carrier for microwave (MW) feeding through.

The generation of V_B^- centers was further confirmed with the GS ODMR. The ODMR spectra were acquired by repeating the measurement cycles 100 000 times while recording the photon counts when the MW is periodically switched on (I_{on}) and off (I_{off}). Both the on and off durations last 10 μs each time (Fig. S1a [37]). The contrast was calculated by I_{on}/I_{off}. The RT ODMR spectrum gives $D_{GS} = 3460$ MHz and $E_{GS} = 49$ MHz, as shown in Fig. 1(d). Both the emission and ODMR spectra are in good agreement with other reports [20,26,38]. Compared to the RT ODMR spectrum, the center frequency of GS ODMR (D_{GS}) blueshifted to 3684 MHz at cryogenic temperatures, consistent with previous work [26,33]. Most importantly, at 7 K, we observed dips other than GS splitting ranging from 2000 to 2600 MHz [light gold shadow in Fig. 1(d)], which we attribute to the ZFS of the V_B^- centers in the ES, as further confirmed by the following experiments.

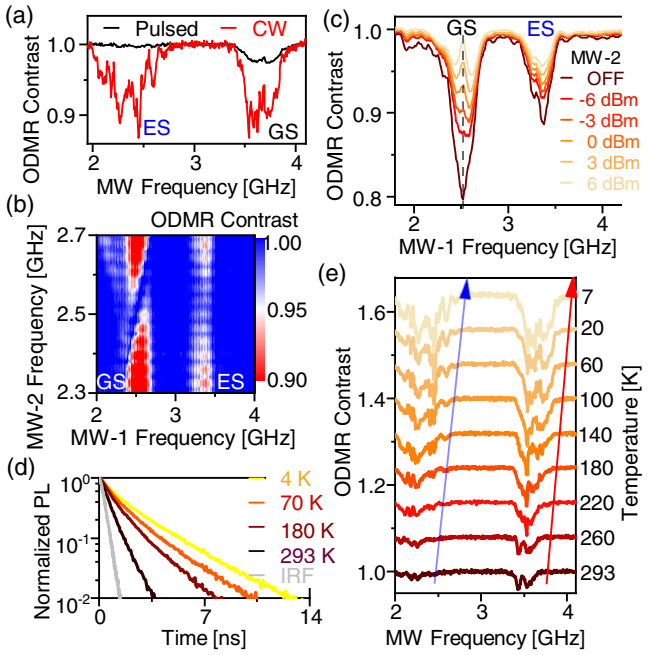

FIG. 2. (a) ODMR spectra of V_B^- centers under pulsed laser-MW excitation (black) and CW laser-MW excitation (red). (b) GS ODMR and ES ODMR spectra (under an external B field of 400 G) while sweeping an additional MW-2. The discontinuous signals of GS ODMR and ES ODMR are due to the large frequency step size of MW2. (c) ES ODMR at different MW-2 power. The MW-2 frequency is fixed at 2520 MHz. (d) Lifetimes of V_B^- centers at different temperatures. The IRF refers to the instrument response function that is much shorter than the lifetime. (e) Temperature-dependent GS ODMR and ES ODMR of V_B^- centers. The two arrows guide the shifting splitting energy as varying the temperatures.

We first confirm the nature of the ODMR dip around 2351 MHz by conducting pulsed ODMR measurement at 7 K [Fig. 2(a)]. The critical point is to inject the MW after all populations relax into the ground state [35,39], and then compare the pulsed ODMR with the continuous wave (CW) ODMR. Experimentally, we first initialized most V_B^- centers to the $m_s = 0$ state with a 5 μs laser pulse. We then apply a 1 μs MW pulse after a dwell time of 500 ns to ensure the complete relaxation of electrons to the GS (Fig. S1b [37]). The spin state after the MW operation is read out with another 5 μs laser pulse. Therefore, in pulsed ODMR, only the MW fields that are resonant with the GS splitting can interact with the system and lead to an ODMR dip. Both CW ODMR and pulsed ODMR resulted in a dip at the GS splitting, while only CW ODRM showed the dip at the ES splitting [Fig. 2(a)], underscoring the nature of this dip around 2351 MHz as the ES splitting.

To confirm that the GS ODMR and ES ODMR signals are originated from the same defects, we performed a two MW experiment. Compared to the CW ODMR, an additional MW2 is applied continuously to create spin mixing in the GS (Fig. S1c [37]). This spin mixing would affect the ES ODMR contrast. Since the ES and GS ODMR fringes in

Fig. 2(a) are very broad, we applied a 400 G magnetic field to split the transitions between $m_s = 0$ and $m_s = \pm 1$ states, resulting in a GS transition ($0 \leftrightarrow -1$) near 2500 MHz and an ES transition ($0 \leftrightarrow +1$) near 3300 MHz. When the MW-2 is parked near resonance with the GS transition, the hole burning effect is observed for the GS ODMR fringes; meanwhile, the ES ODMR contrast is reduced due to the spin depolarization of $m_s = 0$ [Fig. 2(b)]. We also monitor how the ES ODMR contrast changes while the MW-2 power is increased [Fig. 2(c)]. At the highest power of MW-2, the ES ODMR contrast is maximally reduced. These results indicate that the GS and ES signals in Fig. 2(a) are associated with the same type of defects.

The fluorescence lifetime of the ES is vital for ES ODMR as a longer lifetime provides a longer time window for spin rotation in the ES [39]. Below we explain how the lifetime determines the ES ODMR contrast with the help of the sequences for the ES ODMR experiment. First, the spins of V_B^- centers are mostly polarized by off-resonance pumping to the $m_s = 0$ GS. After spin-conserved off-resonance excitation, the MW starts to swap population between the $m_s = 0$ and $m_s = \pm 1$ states in the ES. The more population is transferred from the $m_s = 0$ state to the $m_s = \pm 1$ states, the more the PL intensity is reduced. Therefore, under weak MW power, a longer lifetime of ES can lead to more populations in the dark state, which will eventually lead to a more profound contrast in ES ODMR.

To measure the relationship between the ES lifetime and the ES ODMR contrast, we investigated them at different temperatures. Figure 2(d) shows the ES lifetimes of the V_B^- centers at different temperatures. The lifetime of ES can be extended from the RT value of 0.67 to 2.32 ns at 4 K. The enhancement factor is consistent with other reports [32]. This prolongment is likely due to the modification of nonradiative transitions.

We then measured the ODMR contrast as a function of temperature. The lowest GS ODMR dip amplitude increases from 4% to 12% when the temperature decreases from 293 to 7 K [Fig. 2(e)]. The D_{GS} shows a blueshift of about 200 MHz while decreasing temperature. The temperature-dependent GS ODMR contrast and D_{GS} shift agree well with other reports [26]. Similar trends are observed for ES ODMR, i.e., an increase of the lowest dip from ~2% at 293 K to 12% at 7 K. Moreover, the normalized areas formed by both GS and ES ODMR curves grow steadily during the cooling process (Table S1 [37]). We noticed that the ODMR contrasts in these measurements are limited by the available MW power rather than by physical limits. Unlike NV^- centers in diamond, whose ES ODMR quenches at 6 K due to the lack of dynamic Jahn-Teller effect [40], the V_B^- centers exhibit the maximum ODMR contrast at the lowest achievable temperature. The GS ODMR spectra exhibit fine structures due to the coupling between V_B^- centers and nearby nitrogen nuclear spins [20]. Interestingly, the ES ODMR also exhibits modulated

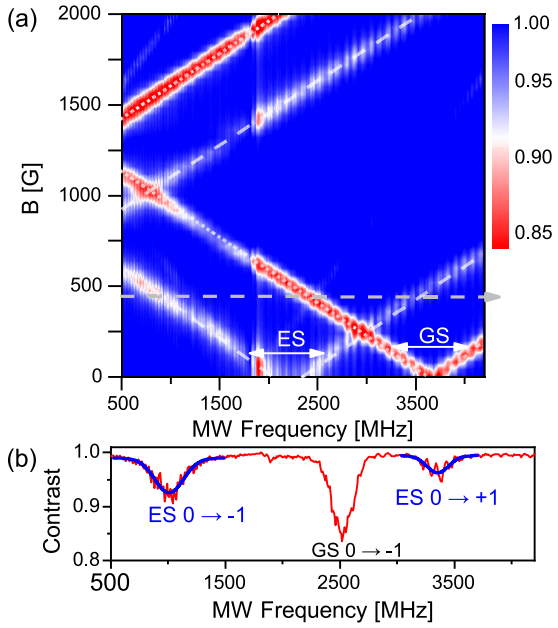

FIG. 3. (a) Low-temperature B field-dependent GS ODMR and ES ODMR spectra. Dashed lines are the guidelines for ES ODMR resonance frequency. The dotted line is the guide for GS ODMR. (b) ODMR line cut at 400 G, gray lines in (a). The blue curves are the Gaussian fit of the two ES transitions ($m_s = 0$ to $m_s = \pm 1$).

fringes throughout the test temperatures. These fine structures may be related to hyperfine interactions between the electron and the nearby nuclear spins.

Next, we studied the response of V_B^- centers to the external magnetic field at cryotemperature. Here, the external magnetic field is applied nearly perpendicular to the surface of the h-BN. As shown in Fig. 3(a), both GS ODMR and ES ODMR signals show the same slope as the B field, inferring the same g factor ($g \sim 2$) for the ES and GS [20]. It indicates that the electron spin dominantly contributes to the g factor while the orbital part contribution is negligible. The D_{ES} is estimated by drawing a line cut at 400 G [Fig. 3(b)] and is attributed to the center frequency of two ES transitions [ES $m_s = 0$ to $m_s = \pm 1$ in Fig. 3(b)] at 2160 MHz. By increasing the magnetic field along the c axis of the V_B^- centers, the $m_s = -1$ state is brought close to the $m_s = 0$ state, resulting in turning points in both ES and GS [41,42]. Based on ODMR spectra, the turning points for the ES and GS are estimated to be 800 and 1330 G [Fig. 3(a)], respectively, which agrees with the experimental results from D_{ES} and D_{GS}.

With the known parameters for g factor and ZFS in the GS and ES, we then determined the eigenstates of V_B^- centers by employing the Hamiltonian described in Supplemental Material, Sec. E [37], neglecting interactions with nuclear spins [23]. When the external magnetic along the c axis of the V_B^- centers increases, the eigenenergy of $|-1\rangle$ states is getting close to the eigenenergy of $|0\rangle$

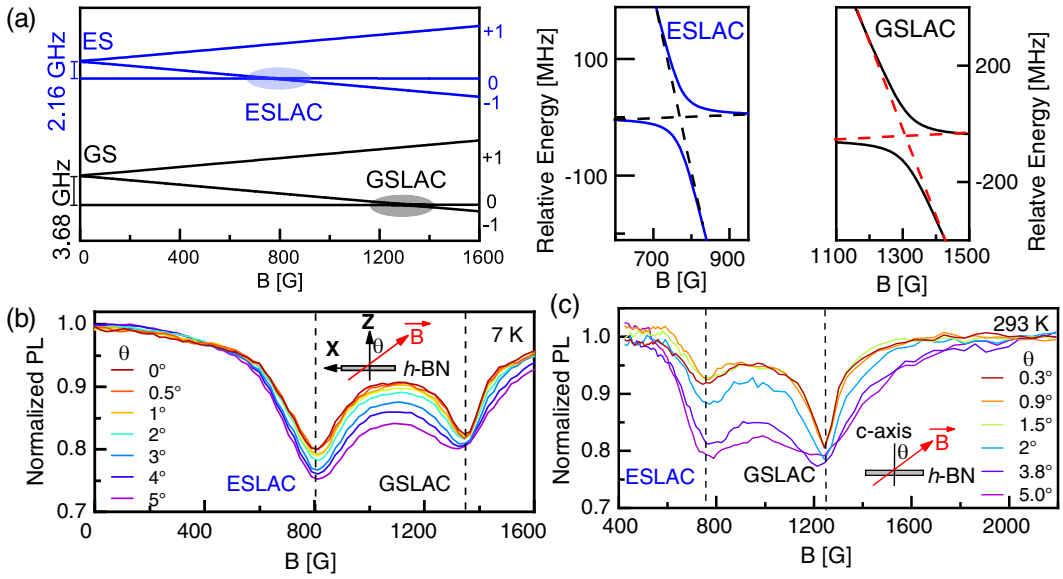

FIG. 4. (a) Energy level diagram of V_B^- centers under a tilted external magnetic field (2°) with respect to the c axis of the sample. Two LAC magnetic fields between $m_s = 0$ and $m_s = -1$ are highlighted in the blue shaded ellipse for the ES and the black shaded ellipse for the GS. The hyperfine interactions are not included in the simulation. Insets show a close-up view of the crossing points near ESLAC (middle) and GSLAC (right). The relative frequencies are obtained by deducting the frequencies at 769 G and at 1307 G. In the simulation, $D_{GS} = 3680$ MHz, $E_{GS} = 50$ MHz, and $D_{ES} = 2160$ MHz, $E_{ES} = 78$ MHz are employed. Normalized magnetic field-dependent emission count rate at 7 K (b) and 293 K (c). The emission count rate is normalized to emission at 0 G for (b) and at 2200 G for (c). In (b), the angle is defined between the magnetic field in the X-Z plane and Z axis. There is a B_y component due to the 2° sample tilting in the Y-Z plane. In (c), the alignment uncertainty is 0.05°.

[Fig. 4(a) shadow regions]. This results in LAC points in the ES and GS [crossing points of black and red dotted lines in Fig. 4(a)]. According to the calculation, the LAC in ES occurs at 769 and 1307 G in GS, respectively [Fig. 4(a)].

To characterize the LACs, we conducted a MW-free experiment, by recording the emission intensity at different magnetic fields. Spin mixing between the bright ($m_s = 0$) and dark ($m_s = -1$) states in either ES or GS due to the transverse magnetic field, strain, or hyperfine interaction [43–45], would reduce the emission rates since the spin populations are transferred from the bright to the dark state. The emission rates change is most evident when the energy difference between these two states is smallest, i.e., when the external magnetic fields are set to be near the ESLAC or GSLAC.

We investigated the magnetic field-dependent emissions at both 7 and 293 K. At both temperatures, PL intensity drops are observed in the vicinity of the ESLAC and GSLAC [Figs. 4(b) and 4(c)]. This temperature-dependent feature near ESLAC is in stark contrast to NV^- centers in diamond. For NV^- centers, the emission reduction near the ESLAC observed at room temperature disappears below 25 K due to a non-negligible contribution of the spin-orbit interaction [43,46], which complicated the dynamic nuclear polarization (DNP) via ESLAC at cryotemperature [41]. The retained emission reduction of V_B^- centers near the ESLAC at cryo-temperature is consistent with the observation of ES ODMR. Both results indicate that the triplet ES of V_{B^-} centers is maintained throughout the working temperature. This fact highlights the possibility of realizing DNP with V_B^- defects even at cryotemperature.

We also looked into how the PL intensity changes at different misalignment angles. A larger misalignment angle (a larger transverse magnetic field) generally leads to a more significant PL intensity reduction near the GSLAC and ESALC along with wider dips, which are also corroborated in Figs. 4(b) and 4(c). However, all curves under different angles θ exhibited two local maximum PL reductions near the same magnetic fields, enabling the estimation of LAC magnetic fields in the ES and GS. We thus estimated $D_{ES} \sim 2240$ MHz and $D_{GS} \sim 3774$ MHz at 7 K, $D_{ES} \sim 2117$ MHz, and $D_{GS} \sim 3472$ MHz at 293 K. Moreover, the magnetic field dependent emission spectra at 7 K exhibit less sensitivity to the tilting angle than those at 293 K. The magnitudes of the emission drops and the width of dips near the ESLAC and GSLAC show slight changes while tilting the angle varies from 0° to 5° at 7 K. However, at 293 K, while the PL intensity drops near the GSLAC are almost unchanged, the corresponding widths changed drastically; by contrast, the drastic change near the ESLAC drops is the emission counts.

In conclusion, we have investigated both room- and low-temperature ES spectroscopies of the V_B^- centers in h-BN. The ES splitting D_{ES} is estimated to be ~2160 MHz at 7 K and ~2117 MHz at 293 K. The ES ODMR contrast is

greater at cryogenic temperature due to longer fluorescence lifetimes at low temperatures. The ES is an important resource for manipulating nearby nuclear spins [36,47]. Knowledge of the energy levels of the ES provides the opportunity to realize DNP. The existence of ESLAC at cryotemperature provides a route toward nuclear spin manipulation at low temperatures.

Even though we know the ZFS of the ES, the realization of nuclear spin polarization via ESLAC remains a challenge. The potential challenges involve the smaller ratio of intersystem crossing rate from the ES manifolds to the singlet state [48,49], the unknown hyperfine interaction in the ES, the exact energy levels in the ES, and the unknown spin-polarization mechanism. The symmetry of the V_B^- centers system would be reduced due to the presence of the strain [31]. The symmetry dictates the energy structures of the V_B^- centers and affects the spin-polarization mechanism [31]. Depending on whether electron spins are polarized into the $m_s = 0$ or $m_s = \pm 1$ states, the nuclear spin would be polarized into different states and the degree of polarization would be affected. In this regard, resonant optical addressing of a single V_B^- center could be vital to reveal the detailed energy levels in the ES and to clarify the interaction between nuclear spins and electron spin [40]. Moreover, the coherent manipulation of the ES would shed light on the spin-dependent relaxation rates from the ES [50]. After knowing these, the nuclear spin polarization could be conceived.

We acknowledge the Singapore National Research Foundation through QEP Grants No. NRF2021-QEP2-01-P02, No. NRF2021-QEP2-03-P01, No. NRF2021-QEP2-03-P10, No. 2019-0643 (QEP-P2), and No. 2019-1321 (QEP-P3), and Singapore Ministry of Education [No. MOE2016-T3-1-006 (S)], the Australian Research council (via CE200100010), the Asian Office of Aerospace Research and Development Grant No. FA2386-17-1-4064 and Office of Naval Research Global N62909-22-1-2028.

*These two authors contributed equally to this work
†igor.aharonovich@uts.edu.au
‡wbgao@ntu.edu.sg

[1] D. D. Awschalom, R. Hanson, J. Wrachtrup, and B. B. Zhou, Nat. Photonics **12**, 516 (2018).
[2] M. H. Abobeih, J. Cramer, M. A. Bakker, N. Kalb, M. Markham, D. J. Twitchen, and T. H. Taminiau, Nat. Commun. **9**, 2552 (2018).
[3] F. J. Heremans, C. G. Yale, and D. D. Awschalom, Proc. IEEE **104**, 2009 (2016).
[4] G. Wolfowicz, F. J. Heremans, C. P. Anderson, S. Kanai, H. Seo, A. Gali, G. Galli, and D. D. Awschalom, Nat. Rev. Mater. **6**, 906 (2021).
[5] J. Choi *et al.*, Proc. Natl. Acad. Sci. U.S.A. **117**, 14636 (2020).
[6] C. Osterkamp, P. Balasubramanian, G. Wolff, T. Teraji, M. Nesladek, and F. Jelezko, Adv. Quantum Technol. **3**, 2000074 (2020).
[7] M. Block, B. Kobrin, A. Jarmola, S. Hsieh, C. Zu, N. L. Figueroa, V. M. Acosta, J. Minguzzi, J. R. Maze, D. Budker, and N. Y. Yao, Phys. Rev. Applied **16**, 024024 (2021).
[8] D. Simin *et al.*, Phys. Rev. X **6**, 031014 (2016).
[9] C. E. Bradley, J. Randall, M. H. Abobeih, R. C. Berrevoets, M. J. Degen, M. A. Bakker, M. Markham, D. J. Twitchen, and T. H. Taminiau, Phys. Rev. X **9**, 031045 (2019).
[10] C. Babin *et al.*, Nat. Mater. **21**, 67 (2022).
[11] R. Fukuda *et al.*, New J. Phys. **20**, 083029 (2018).
[12] F. Shi *et al.*, Science **347**, 1135 (2015).
[13] T. Song *et al.*, Science **374**, 1140 (2021).
[14] B. B. Zhou, P. C. Jerger, K.-H. Lee, M. Fukami, F. Mujid, J. Park, and D. D. Awschalom, Phys. Rev. X **10**, 011003 (2020).
[15] A. Gao *et al.*, Nature (London) **595**, 521 (2021).
[16] X. Liu and M. C. Hersam, Nat. Rev. Mater. **4**, 669 (2019).
[17] G. Grosso, H. Moon, B. Lienhard, S. Ali, D. K. Efetov, M. M. Furchi, P. Jarillo-Herrero, M. J. Ford, I. Aharonovich, and D. Englund, Nat. Commun. **8**, 705 (2017).
[18] C. Fournier *et al.*, Nat. Commun. **12**, 3779 (2021).
[19] N. Chejanovsky *et al.*, Nat. Mater. **20**, 1079 (2021).
[20] A. Gottscholl *et al.*, Nat. Mater. **19**, 540 (2020).
[21] H. L. Stern, Q. Gu, J. Jarman, S. E. Barker, N. Mendelson, D. Chugh, S. Schott, H. H. Tan, H. Sirringhaus, I. Aharonovich, and M. Atatüre, Nat. Commun. **13**, 618 (2022).
[22] A. L. Exarhos, D. A. Hopper, R. N. Patel, M. W. Doherty, and L. C. Bassett, Nat. Commun. **10**, 222 (2019).
[23] A. Gottscholl, M. Diez, V. Soltamov, C. Kasper, A. Sperlich, M. Kianinia, C. Bradac, I. Aharonovich, and V. Dyakonov, Sci. Adv. **7**, eabf3630 (2021).
[24] W. Liu *et al.*, arXiv:2101.11220
[25] X. Gao *et al.*, Nano Lett. **21**, 7708 (2021).
[26] W. Liu *et al.*, ACS Photonics **8**, 1889 (2021).
[27] X. Gao, S. Pandey, M. Kianinia, J. Ahn, P. Ju, I. Aharonovich, N. Shivaram, and T. Li, ACS Photonics **8**, 994 (2021).
[28] F. F. Murzakhanov *et al.*, Nanomaterials (Basel)**11**, 1373 (2021).
[29] A. Zobelli, A. Gloter, C. P. Ewels, G. Seifert, and C. Colliex, Phys. Rev. B **75**, 245402 (2007).
[30] J. Kotakoski, C. H. Jin, O. Lehtinen, K. Suenaga, and A. V. Krasheninnikov, Phys. Rev. B **82**, 113404 (2010).
[31] V. Ivády, G. Barcza, G. Thiering, S. Li, H. Hamdi, J.-P. Chou, Ö. Legeza, and A. Gali, npj Comput. Mater. **6** (2020).
[32] J. R. Reimers, J. Shen, M. Kianinia, C. Bradac, I. Aharonovich, M. J. Ford, and P. Piecuch, Phys. Rev. B **102**, 144105 (2020).
[33] A. Gottscholl, M. Diez, V. Soltamov, C. Kasper, D. Krauße, A. Sperlich, M. Kianinia, C. Bradac, I. Aharonovich, and V. Dyakonov, Nat. Commun. **12**, 4480 (2021).
[34] M. Huang *et al.*, arXiv:2112.13570.
[35] G. D. Fuchs, V. V. Dobrovitski, R. Hanson, A. Batra, C. D. Weis, T. Schenkel, and D. D. Awschalom, Phys. Rev. Lett. **101**, 117601 (2008).

[36] V. Jacques, P. Neumann, J. Beck, M. Markham, D. Twitchen, J. Meijer, F. Kaiser, G. Balasubramanian, F. Jelezko, and J. Wrachtrup, Phys. Rev. Lett. **102**, 057403 (2009).
[37] See Supplemental Material at http://link.aps.org/supplemental/10.1103/PhysRevLett.128.216402 for sample preparation, experimental setup description, laser and microwave pulse sequences design, and the simplified modeling of the eigenenergy of V_B^- centers under external magnetic fields.
[38] N. Mendelson *et al.*, Adv. Mater. **34**, 2106046 (2022).
[39] P. Neumann, R. Kolesov, V. Jacques, J. Beck, J. Tisler, A. Batalov, L. Rogers, N. B. Manson, G. Balasubramanian, F. Jelezko, and J. Wrachtrup, New J. Phys. **11** (2009).
[40] A. Batalov, V. Jacques, F. Kaiser, P. Siyushev, P. Neumann, L. J. Rogers, R. L. McMurtrie, N. B. Manson, F. Jelezko, and J. Wrachtrup, Phys. Rev. Lett. **102**, 195506 (2009).
[41] R. Fischer, A. Jarmola, P. Kehayias, and D. Budker, Phys. Rev. B **87**, 125207 (2013).
[42] A. L. Falk, P. V. Klimov, V. Ivady, K. Szasz, D. J. Christle, W. F. Koehl, A. Gali, and D. D. Awschalom, Phys. Rev. Lett. **114**, 247603 (2015).
[43] L. J. Rogers, R. L. McMurtrie, M. J. Sellars, and N. B. Manson, New J. Phys. **11**, 063007 (2009).
[44] X. F. He, N. B. Manson, and P. T. H. Fisk, Phys. Rev. B **47**, 8809 (1993).
[45] R. J. Epstein, F. M. Mendoza, Y. K. Kato, and D. D. Awschalom, Nat. Phys. **1**, 94 (2005).
[46] M. L. Goldman, A. Sipahigil, M. W. Doherty, N. Y. Yao, S. D. Bennett, M. Markham, D. J. Twitchen, N. B. Manson, A. Kubanek, and M. D. Lukin, Phys. Rev. Lett. **114**, 145502 (2015).
[47] V. Ivády, K. Szász, A. L. Falk, P. V. Klimov, D. J. Christle, E. Janzén, I. A. Abrikosov, D. D. Awschalom, and A. Gali, Phys. Rev. B **92**, 115206 (2015).
[48] S. Baber, R. N. Malein, P. Khatri, P. S. Keatley, S. Guo, F. Withers, A. J. Ramsay, and I. J. Luxmoore, Nano Lett. **22**, 461 (2022).
[49] L. Busaite, R. Lazda, A. Berzins, M. Auzinsh, R. Ferber, and F. Gahbauer, Phys. Rev. B **102**, 224101 (2020).
[50] G. D. Fuchs, V. V. Dobrovitski, D. M. Toyli, F. J. Heremans, C. D. Weis, T. Schenkel, and D. D. Awschalom, Nat. Phys. **6**, 668 (2010).